Nano Research

Open Access

Research Article

Synergistic regulation of morphology and electronic coupling of dual-ligand NiFe MOF for efficient electrocatalysis in multi-electrolyte water splitting

Shuyan Fan, Xinping Han, Ling Li, Yan Xu, Wenyue Gao, Yan Zhang, Zhu Gao, and Cuijuan Wang ✉

School of Chemistry, Southwest Jiaotong University, Chengdu 610031, China

Cite this article: *Nano Research*, **2025**, *18*, 94907305. https://doi.org/10.26599/NR.2025.94907305

ABSTRACT: Our study achieves efficient electrocatalysis for the electrooxidation reaction in multi-electrolyte systems by synergistically modulating structure and electronic coupling through rational design. We establish novel principles for controlling the morphology and performance of metal-organic frameworks (MOFs): Formation of nano-flower structure requires co-existence of Ni site and Fc ligand, doping of Fe sites promotes three-dimensional (3D) crystal morphology development, which marks a pioneering advance in the field. Among them, the bimetallic dual-ligand MOF: NiFe-BDC/Fc (NFBF)(6:2) exhibits outstanding electrocatalytic performance (210 mV at 10 mA·cm^{-2}). *Operando* Raman spectroscopy and X-ray absorption fine structure (XAFS) reveal the electronic restructuring feature of NFBF(6:2) during the catalytic oxygen evolution reaction (OER) process. Combined with density functional theory (DFT) calculations, which identify Ni as the catalytic active site, these investigations uncover significant electronic migration and redistribution, substantially reducing the reaction energy barrier and accelerating the catalytic process. Comprehensive exploration demonstrates that NFBF(6:2) not only performs well under various multi-electrolyte conditions but also maintains a nearly consistent catalytic mechanism. Furthermore, when applied to overall water splitting, (+) NFBF(6:2) || NFBF(6:2) (−) achieves significant catalytic effects in both alkaline freshwater (1.40 V at 10 mA·cm^{-2}) and seawater (1.44 V at 10 mA·cm^{-2}) electrolyzers. This work highlights the crucial role of electronic coupling in optimizing electrocatalytic performance and offers new insights for addressing mitigating environmental pollution, embodying substantial practical and research potential.

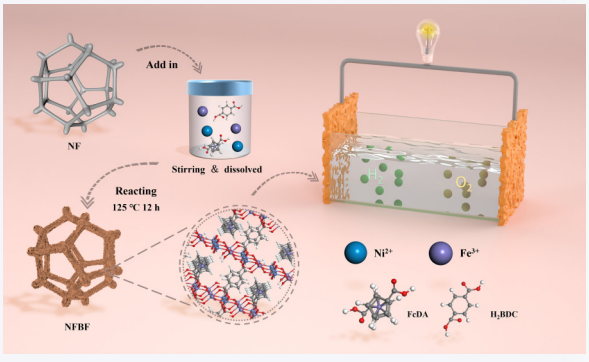

KEYWORDS: metal-organic frameworks, oxygen evolution, electrocatalysts, overall water splitting

1 Introduction

In recent years, with the acceleration of population growth and urbanization, there has been a continuous increase in demand for energy, prompting countries worldwide to advocate for sustainable development. To combat climate change [1–3], China has set forth national strategic goals of "peaking carbon emissions by 2030 and achieving carbon neutrality by 2060". Hydrogen energy, with its high energy density and the advantage of generating water upon combustion, serves as a promising energy carrier for carbon reduction and sustainable development [4–6]. Pollution-free hydrogen energy is particularly crucial in the clean energy landscape of the 21st century. As environmental conditions continue to deteriorate, freshwater resources face severely escalating threats of pollution and depletion. Meanwhile, seawater, accounting for over 96% of the world's water resources, stands as one of the most abundant resources. If utilized effectively, it holds the potential to save a significant amount of freshwater. Similarly, industrial production generates a substantial amount of wastewater with varying urea content. The reuse of such wastewater can simultaneously address environmental pollution issues such as acid rain resulting from its disposal [7–10].

Among various hydrogen production strategies, electrochemical water splitting has emerged as one of the most attractive and efficient methods for clean hydrogen production in recent years [11–14]. The oxygen evolution reaction (OER) in electrochemical water splitting is the complementary half-reaction to hydrogen evolution reaction (HER). As a four-electron-proton coupled

Received: January 14, 2025; **Revised:** February 12, 2025
Accepted: February 13, 2025

✉Address correspondence to wangcuijuan@swjtu.edu.cn

reaction, OER involves complex mechanisms and exhibits sluggishly slow reaction kinetics, resulting in high overpotentials, which is a critical limiting factor for the efficiency of electrolytic hydrogen production. Improving the efficiency and durability of OER catalysts directly impacts the efficiency and cost-effectiveness of catalysts [15, 16]. Meanwhile, seawater electrolysis encounters influential hurdles, such as competing chlorine evolution reaction (ClER) at the anode during OER, and toxicity corrosion from high concentrations of Cl^- on electrocatalysts alike [17–20]. While urea oxidation reaction (UOR) functions as a promising alternative to OER, its inherent instability and sluggish electro kinetics persist as challenges awaiting resolution.

Metal-organic frameworks (MOFs) are ordered crystalline structures formed by linking metal nodes with organic ligands [21]. In the design of OER electrocatalysts, Ni-based MOFs have been extensively studied and utilized as modification foundations due to their excellent catalytic activity [22]. Various research endeavor shave explored incorporating different metal nodes [23], altering ligand environments [24], doping compounds [25] or single atoms [26].

Taking advantage of the flexibility of MOFs, a plethora of electrocatalysts have surfaced in recent years, originating from MOFs as design points: Hu formulated a trimetallic electrocatalyst, CoNiFc-MOF, featuring diminished energy barriers and improved conductivity [27]. CoBDC FcCA have been synthesized by partially substituting ligands, where FcCA forms a tension-strained microreactor, regulating the antibonding states of Co 3d and O 2p orbitals, and accelerating the reaction kinetics of the entire OER process [28]. NiFeMOF@Ni_2P/Ni $(OH)_2$ nanoplate arrays on nickel foam (NF) effectively promote the adsorption of OH* and OOH*, thereby expediting the overall reaction kinetics and enhancing the performance of OER in seawater environments [29]. Li proposed a three-dimensional (3D) self-supporting layered nanoarray electrode (CC/MnNi@NC), facilitating the generation of active Ni^{3+} species and promoting the rate-determining step (RDS) *COO intermediate desorption, significantly advancing the electrocatalytic performance of UOR [30].

Although significant progress has been made in current research, the focus of most studies remains on prioritizing the application of single-environment electrocatalysts. Building upon our previous investigation [31, 32], if there exists an electrocatalyst capable of addressing the issues of toxicity and instability in non-freshwater electrolytes, satisfying multiple environmental electrocatalysis scenarios while exhibiting significant performance, then the expansion of electrocatalytic materials' applications and environmental protection would be highly beneficial. Herein, in Fig. 1, we have designed a NFBF MOF material with multi-environment adaptability for electrocatalytic water splitting. This MOF comprises Ni and Fe metal sites, with organic linkers of terephthalic acid (H_2BDC) and ferrocenedicarboxylic acid (FcDA). We tested its OER performance in various conditions: in regular alkaline conditions (1 M KOH), in a simulated urine electrolyte environment (1 M KOH + 0.33 M Urea), in simulated seawater (1 M KOH + 0.5 M NaCl, 1 M KOH + 1 M NaCl), and under actually real seawater conditions. The optimal performing NFBF(6:2) exhibited the lowest overpotentials at 10 $mA{\cdot}cm^{-2}$, which were 210, 140, 220, 240, and 280 mV, respectively, outperforming other catalysts under the same electrolyte conditions.

Furthermore, we explored a series of rules governing the synergistic regulation and modulation of structure and performance when designing and synthesizing MOF electrocatalytic materials. By leveraging these rules, we identified the NFBF(6:2) structure with superior performance, which BDC: FcDA = 6:2. Moreover, the (+) NFBF(6:2) || NFBF(6:2) (−) system exhibited remarkable performance in alkaline freshwater and seawater electrolyzers. At low voltages of 1.40, 1.56, and 1.67 V, it could drive current densities of 10, 50, and 100 $mA{\cdot}cm^{-2}$, respectively, in the electrolysis cell. Through *operando* Raman spectroscopy, X-ray absorption fine structure (XAFS), and density functional theory (DFT) calculations, we demonstrated the following: 1) the beneficial decrease in electron density around Ni on NFBF(6:2), promoting the adsorption of oxygen intermediates at Ni active sites; 2) electron transfer to Fe^{3+} and organic ligands, enhancing conductivity; 3) the inclusion of ferrocene ligands facilitating the exposure of Ni active sites. This work might promote a deep understanding of the efficient multienvironment water splitting reaction.

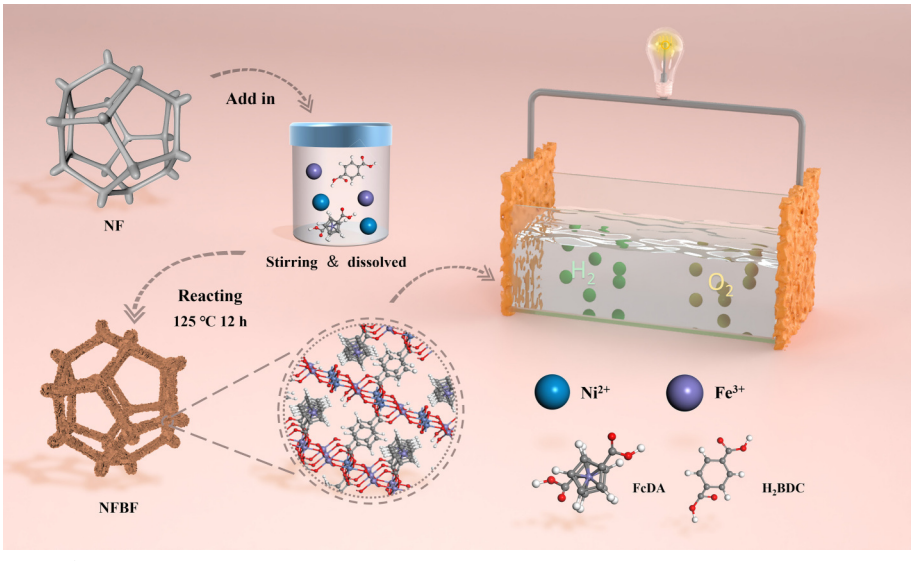

Figure 1 Illustration of NFBFs synthesis.

2 Results and discussion

2.1 OER electrochemical performance of NFBF

Firstly, we modified the existing MOFs NiFe-BDC (NFB), the NFB comprises Ni and Fe metal sites, with organic linkers of H_2BDC. The relevant synthesis methods are described in detail in "Methods" section. Briefly, with the addition ratio of Ni and Fe fixed, we introduced the FcDA and set the addition ratios of the original terephthalic acid ligand (BDC) to FcDA as 3:5, 1:1, 5:3, and 6:2, respectively, which were named NFBF(3:5), NFBF(1:1), NFBF(5:3), and NFBF(6:2). "NFBF" comprises Ni and Fe metal sites, with organic linkers of H_2BDC and FcDA. These modified MOFs were then applied to the electrocatalytic OER system, and we compared their performance with that of NFB.

Implementing a typical three-electrode electrochemical setup, the electrocatalytic activity of the MOFs towards OER was evaluated in 1.0 M KOH aqueous solution at 25 °C employing linear sweep voltammetry (LSV). Figure 2(a) depicts the polarization curves comparing the performance of the best-performing NFBF(6:2) sample with the unmodified NFB and the base NF [33]. At current densities of 10, 50, and 100 mA·cm^{-2}, NFBF(6:2) exhibited low overpotentials of 210, 232, and 240 mV, respectively, while the unmodified NFB showed overpotentials of 241, 281, and 311 mV at the same current densities in terms of overpotential. Additionally, we compared the overpotential of standard commercial RuO_2. Comparatively, RuO_2/NF showed an overpotential of 370 mV at a current density of 50 mA·cm^{-2}, which is 138 mV higher than that of NFBF. It also affects a significant improvement compared NF, further underscoring the superiority of NFBF in OER electrocatalysis.

In parallel comparison of the performance of NFBF materials with different ratios, as shown in Fig. S1 in the Electronic Supplementary Material (ESM), NFBF(5:3), NFBF(1:1), and NFBF(3:5) indicated overpotentials of 233, 237, and 257 mV, respectively, at a current density of 50 mA·cm^{-2}.

Furthermore, the Tafel slope symbolizes the relationship between OER reaction rate and overpotential, where a lower Tafel slope denotes lower overpotential requirement for achieving higher performance, thereby signifying favorable reaction kinetics [34]. As illustrated in Fig. 2(b) and Fig. S2 in the ESM, the Tafel slope observed for NFBF(6:2) stood at 67.2 mV·dec^{-1}, lower than that of other samples. Additionally, the interface resistance of the electrocatalyst was analyzed through electrochemical impedance spectroscopy (EIS). Figure 2(c) and Fig. S3 in the ESM display the Nyquist plots and equivalent circuits of the NFBF(6:2), NFB, RuO_2/NF, and NF, respectively. The charge transfer resistance (R_{ct}) at the electrode/electrolyte interface, along with the polarization resistance (R_p) generated by charge accumulation on the electrode surface jointly determines the chemical reaction rate, both of which are intricately related to the active surface area of the electrode material. Smaller values of R_{ct} and R_p indicate better electrochemical performance of the MOFs [35]. Table S1 in the ESM summarizes the R_p and R_{ct} values as well as other circuit components obtained from fitting. Similarly, during the fitting workings, the diameter of the semicircle in the Nyquist plot can visually compare the R_p values of electrode materials. As seen in Fig. 2(c), the semicircle diameter of NFBF(6:2) is much smaller than that of NFB, RuO_2/NF, and NF, indicating the fastest ion transfer and electron transfer at the NFBF(6:2) electrolyte interface, thus resulting in better OER kinetics. Additionally, a parallel comparison of the semicircle diameters of NFBF materials with different ratios obtained from Fig. S3 in the ESM also leads to the conclusion that NFBF(6:2) has the smallest semicircle diameter. Furthermore, EIS results are consistent with overpotential and Tafel slope values. Hence, based on the aforementioned discussion, NFBF(6:2) with the best OER performance is selected for subsequent discussions.

To further elucidate the enhanced OER electrochemical activity of NFBF(6:2), the electrochemical double-layer capacitance (C_{dl}) was measured to estimate the electrochemically active surface area (ECSA) associated with exposed active sites. As shown in Fig. 2(d) and Fig. S4 in the ESM, C_{dl} was determined by analyzing cyclic

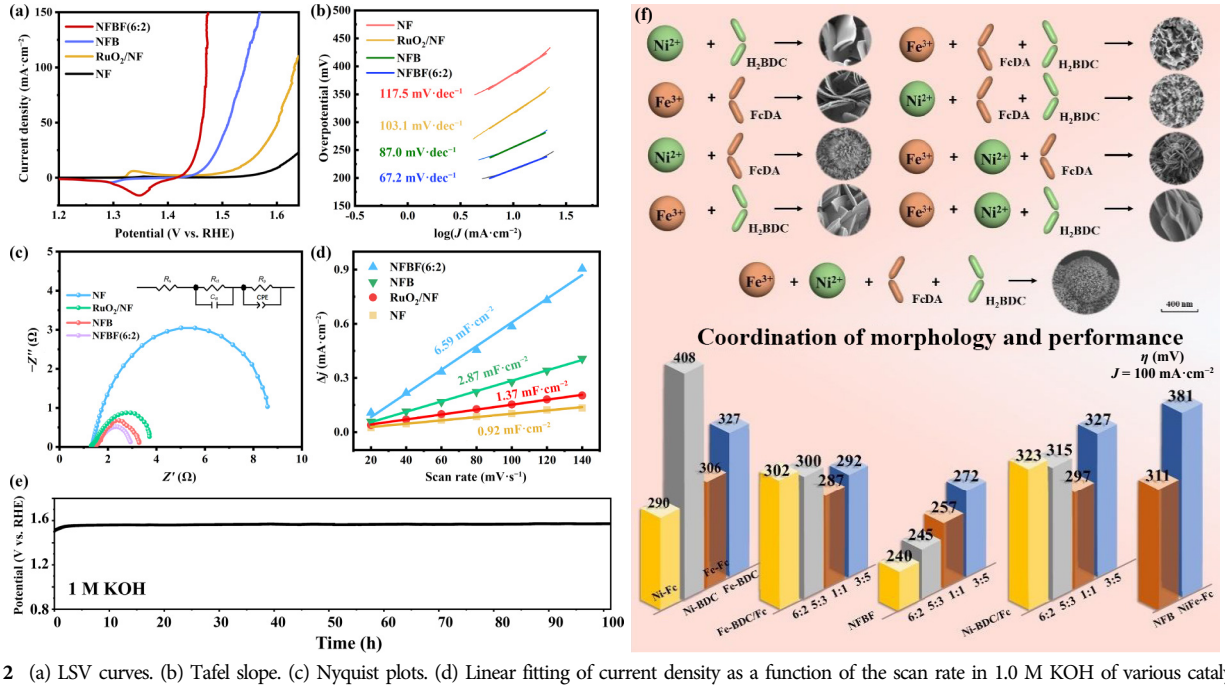

Figure 2 (a) LSV curves. (b) Tafel slope. (c) Nyquist plots. (d) Linear fitting of current density as a function of the scan rate in 1.0 M KOH of various catalysts. (e) Stability test performed at 50 mA·cm^{-2} of NFBF(6:2) in 1 M KOH. (f) Coordination of morphology and performance of different MOFs with different synthesis strategy.

voltammetry (CV) curves obtained at different scan rates, where no discernible oxidation or reduction peaks appeared relative to reversible hydrogen electrode (RHE) between 1.10 and 1.25 V. From the CV curves, the fitted linear slope is directly proportional to ECSA and used to calculate the C_{dl} value of the electrode [36]. The results indicate that the C_{dl} values of the unmodified NFB (2.87 mF·cm^{-2}), RuO_2/NF (1.37 mF·cm^{-2}), and NF (0.92 mF·cm^{-2}) were both lower than that of NFBF(6:2) (6.59 mF·cm^{-2}), suggesting that the NFBF(6:2) electrocatalyst exhibits a greater number of active metal sites exposed on its surface, thus resulting in the highest OER electrocatalytic activity.

For energy conversion systems, besides electrocatalytic performance, the stability of the electrocatalyst is also a key factor [37]. NFBF(6:2) exhibited excellent stability under alkaline conditions of 1.0 M KOH at a current density of 50 mA·cm^{-2}, maintaining its catalytic activity for at least 100 h, as shown in Fig. 2(e), thus demonstrating the outstanding long-term durability of NFBF(6:2).

From this chapter, we can conclude that the modified NFB, referred to as NFBF, indeed exhibits superior electrocatalytic performance for OER. However, this also raises us a further question: Is the notable catalytic performance only achievable when Ni, Fe sites, BDC, and Fc coexist? What are the catalytic properties of MOFs formed by different combinations of sites and ligands, and are there any underlying patterns? These questions will be addressed in the following section.

2.2 Synthesis and morphology control of MOFs

To investigate the electrocatalytic OER performance and potential patterns of MOFs derived from different combinations of Ni and Fe metal sites with BDC and Fc ligands, we focused on the relationship between morphology and performance. This approach aims to uncover the underlying regulatory mechanisms governing their catalytic behavior.

From the synthesis method (Fig. 2(f)), it can be observed that a series of MOFs in this study are all loaded onto NF substrates. As shown in Fig. S5 in the ESM, the scanning electron microscopy (SEM) image of the foam nickel skeleton reveals a smooth surface. As depicted in Fig. 2(f), different doping conditions manifest their unique morphologies.

From Fig. 2(f) and Figs. S6(a) and S6(b) in the ESM, it is witnessed that the morphology of Ni-BDC (single-metal single-ligand) appears as nanosheets, with thin layers and large interspaces, while Fe-BDC in Figs. S6(c) and S6(d) in the ESM manifests as thicker nanosheets or, more accurately, thick nanosheets formed by stacking thin nanosheets. This analysis suggests that the introduction of Fe^{3+} leads to a change in the growth pattern of nanosheets, transitioning from longitudinal plane growth to a more three-dimensional structure. Meanwhile, Ni-Fc in Figs. S6(e) and S6(f) in the ESM evidences a nanoflower morphology, like MOFs obtained with the BDC ligand, comprising dispersed nanosheets but forming a radial structure instead of a planar stack, while Fe-Fc, like BDC, results in stacked nanosheets.

SEM images in Fig. 2(f) and Figs. S7(a) and S7(b) in the ESM reveal that NiFe-BDC (NFB double-metal single-ligand) also signifies a nanosheet morphology, with interconnected layers and uniform distribution, whereas NiFe-Fc (Figs. S7(c) and S7(d) in the ESM) form thicker nanosheet structures, resembling a cactus. Similarly, in Fig. 2(f) and Fig. S8 in the ESM, Ni-BDC/Fc (single-metal double-ligand) also forms nanoflowers resembling those of Ni-Fc, with the "petals" becoming more dispersed as the BDC/Fc ratio shrivels. In contrast, Fe-BDC/Fc (Fig. 2(f) and Fig. S9 in the ESM) does not form nanoflowers but aggregates nanosheets akin to Fe-Fc, analogous to the previous materials, the nanosheets become more dispersed further as the BDC/Fc ratio decreases. Thus, it can be inferred that the formation of nanoflowers requires the presence of both Ni sites and the Fc ligand, indicating a necessary condition.

The SEM image of NiFe-BDC/Fc (NFBF double-metal double-ligand) in Figs. 2(f) and 3, and Fig. S10 in the ESM betokens a distinct nanoflower structure, with the "petals" being more three-dimensional and inclined, suggesting a tendency towards conical shapes comes down to the introduction of Fe sites. This correlates with the earlier analysis. With changes in the BDC/Fc ratio, the morphological changes in NFBF(6:2) (Fig. 3 and Figs. S10(g) and S10(h) in the ESM) are slightly more pronounced, with the nanoflowers growing evenly, and the petals orderly arranged, while as the BDC/Fc ratio increases, the growth of nanoflowers becomes more irregular.

Predicting electrocatalytic performance based on morphology, bimetallic dual-ligand MOFs exhibit radial small prickly nanoflowers, exposing more active sites, facilitating electron transfer, increasing the contact area with the electrolyte, and aiding in the removal of gas bubbles during OER [38], thus enhancing electrocatalytic performance.

Continuing with LSV evaluations at room temperature, single-metal single-ligand Ni (Fe)-BDC (Fc) MOFs (Fig. 2(f) and Fig. S11 in the ESM) show that Ni-Fc has the smallest overpotential (290 mV), attributed to its uniform nanoflower structure. In bimetallic single-ligand NFBF MOFs, the overpotential of NFB is 311 mV, lower than that of NiFe-Fc (381 mV), owing to its thinner nanosheet structure, while the thicker nanosheet morphology of NiFe-Fc has a detrimental effect on electrocatalysis. The single-metal dual-ligand Ni (Fe)-BDC/Fc shows minimal variation in overpotential, and their morphologies tend towards aggregation, thereby resulting in insufficient contact area for the electrocatalyst, ultimately leading to subpar electrocatalytic performance. However, a noticeable trend emerges as the BDC/Fc ratio decreases, the nanosheets become more dispersed, consequently reducing the overpotential. In contrast, bimetallic dual-ligand NFBF exhibits the lowest overpotential (240 mV) and the most superior electrocatalytic performance, intricately linked with its distinctive three-dimensional conical nanoflower morphology. Thus, the obtained overpotential results align with the earlier morphology predictions, further highlighting the synergistic control between the performance and morphology of this series of materials.

Afterall, through the observation and analysis of the morphologies of MOF materials under different combinations of metals and ligands, the principles for controlling the morphology of MOFs are obtained as follows: The formation of a nanoflower structure requires the simultaneous presence of Ni sites and Fc ligands. The doping of Fe sites promotes the development of crystal morphology in a three-dimensional direction. Moreover, the change in the BDC/Fc ratio affects the morphology of MOF materials, and the degree of significance of this ratio's influence on MOF materials with different metal sites varies.

2.3 Characterization of NFBF(6:2)

In the following section, we will focus on discussing the morphology and characterization of the MOF NFBF(6:2), which exhibits optimal performance. First, we further investigated the

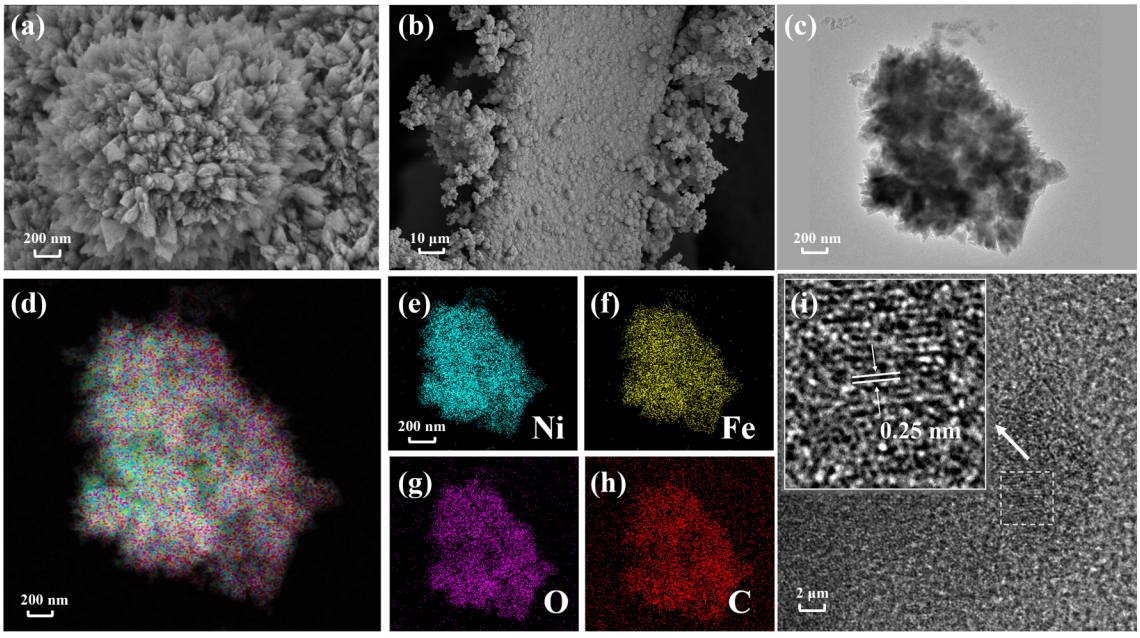

Figure 3 ((a) and (b)) SEM, ((c) and (i)) TEM, and ((d)–(h)) EDS mapping images of NFBF(6:2).

microstructure of the optimal material NFBF(6:2) using transmission electron microscopy (TEM) and high-resolution TEM (HRTEM). TEM image (Fig. 3(c)) revealed the nanoflower morphology at the edges of NFBF(6:2), consistent with SEM observations.

Additionally, HRTEM (Fig. 3(i)) unveiled lattice fringes with a spacing of approximately 0.25 nm, corresponding to the (402) crystal plane of Ni-MOF, as reported in Ref. [39], confirming the successful synthesis of the material. Energy-dispersive X-ray spectroscopy (EDS) results confirmed the uniform distribution of C, O, Fe, and Ni elements within NFBF(6:2) (Figs. 3(d)–3(h)). Furthermore, the atomic ratio of Ni to Fe in NFBF(6:2) was found to be 2:1, in accordance with inductively coupled plasma (ICP) results (Table S2 in the ESM).

Figure 4(a) and Fig. S12 in the ESM display the X-ray diffraction (XRD) pattern of MOFs. Comparing the synthesized XRD diffraction spectrum of NFBF(6:2) with the simulated standard PDF card of Ni-MOF (CCDC: 985792), the characteristic peaks are in good agreement. Specifically, the peaks at 2-Theta of 8.8°, 14.2°, 15.7°, and 17.7° correspond to the (200), (001), (201), and (400) crystal planes, respectively. A noticeable aspect is that regardless of whether Fe is doped at Ni sites or through ligand doping, the main crystal diffraction peaks remain unchanged. This consistency in atomic arrangement and unit size [40], which is in line with the TEM data, serves as a reference for predicting the crystal structure.

The chemical composition and elemental oxidation states of NFBF(6:2) were further characterized using infrared spectroscopy [41], Raman spectroscopy, and X-ray photoelectron spectroscopy (XPS) [42]. The infrared spectrum in Fig. 4(b) shows that both the double-metal double-ligand MOF with different ratios and the pre-modified MOF exhibit asymmetric and symmetric stretching vibration peaks of carboxyl groups at 1580 and 1380 cm^{-1}, respectively. Additionally, a conjugated double bond stretching vibration peak belonging to the aromatic ring appears at 1100 cm^{-1}. Peaks at 814 and 736 cm^{-1} correspond to bending vibration peaks of the benzene ring, while the characteristic peak of the M–O bond appears at 523 cm^{-1}.

However, after the introduction of ferrocene carboxylic acid ligands, a bending peak of ferrocene ring C–H appears at 780 cm^{-1}, and a characteristic peak of the ferrocene aromatic ring appears at 480 cm^{-1}, further confirming the successful synthesis of the MOF. The red shift of the carboxyl group characteristic peak at 1687 to 1580 cm^{-1} further indicates the bonding of the carboxyl group to the metal. Additionally, the characteristic peak at 2400 cm^{-1} correlates with the atmospheric carbon dioxide. Raman spectra (Fig. 4(c)) reveal characteristic peaks of the ferrocene aromatic ring at Raman shifts of 480 and 550 cm^{-1} for the ferrocene ligand and the modified MOF, respectively. Peaks at 630 and 865 cm^{-1} coincide with benzene ring C–H stretching vibrations for all samples, while peaks at 1420 and 1606 cm^{-1} are attributed to inward and outward stretching vibrations of the carboxyl group. Moreover, Raman spectra exhibit a red shift with the formation of coordination compounds, indicating changes in the corresponding peak chemical bonds and confirming the successful synthesis of the MOF. The disappearance of the ligand characteristic peak at 1280 cm^{-1} further indicates the bonding of the carboxyl group to the metal.

XPS was employed to investigate the electronic structure of NFBF(6:2) and NFB. The full XPS survey spectra indicate the presence of Ni, Fe, C, and O elements in both NFBF(6:2) and NFB (Fig. S13 in the ESM). High-resolution Ni 2p XPS spectra confirm the chemical state of Ni ions as Ni^{2+}, with a positive shift of 0.1 eV in the Ni $2p_{3/2}$ peak from 856.0 eV for NFB to 856.1 eV for NFBF(6:2), indicating a change in the electron distribution on Ni and a decrease in electron density (Fig. 4(d)) [43]. Similarly, the Fe 2p XPS spectra show that only Fe^{3+} is presented in NFB, while both Fe^{3+} and Fe^{2+} are detected in NFBF(6:2), demonstrating the successful introduction of the ferrocene ligand (Fig. 4(e)). The negative shift of 0.3 eV in the Fe^{3+} $2p_{3/2}$ peak from 711.2 eV for NFB to 710.9 eV for NFBF(6:2), indicates an increase in electron density around Fe^{3+}. Additionally, the appearance of Fe^{2+} $2p_{3/2}$ and Fe^{2+} $2p_{1/2}$ peaks in NFBF(6:2) at 708.3 and 720.9 eV, respectively, further confirms the successful modification. Notably, as shown in Fig. 4(f), the O 1s peak observed at 531.6 eV for NFBF(6:2) exhibits a 0.1 eV decrease

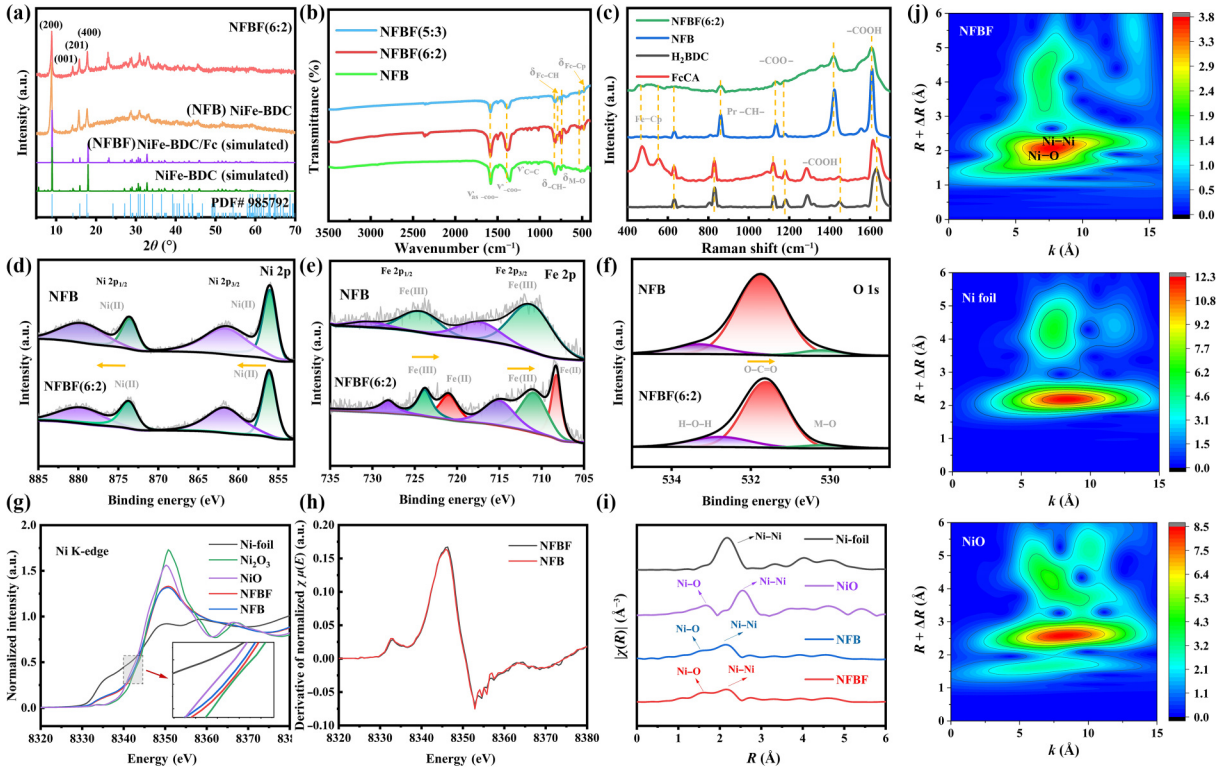

Figure 4 (a) XRD patterns, (b) FTIR and (c) Raman results of different MOFs. High-resolution (d) Ni 2p, (e) Fe 2p, and (f) O 1s XPS spectra of NFBF(6:2) and NFB. (g) Normalized Ni XANES spectra of NFBF(6:2), NFB, and the reference samples. (h) First-order derivative of normalized Ni XANES spectra. (i) Ni-k edge EXAFS spectra and (j) corresponding wavelet-transformed k^3-weighted EXAFS spectra of NFBF(6:2), NFB, and the reference samples.

compared to NFB, indicating a heightened electron density on the organic bridging ligand.

To understand the local information of NFBF(6:2), XAFS spectroscopy was employed. The overall X-ray absorption near-edge structure (XANES) spectrum of NFBF(6:2) is between NiO and Ni_2O_3, closer to Ni_2O_3 (Fig. 4(g)), but weak pre-edge peaks are observed at 8333 eV for both NFBF(6:2) and NFB, corroborating possible lattice distortions and reduced symmetry, which favor electron excitation [22]. Compared with NFB, NFBF(6:2) exhibits a positive shift in the near-edge absorption region (Fig. 4(h)), suggesting an increase in the oxidation state of Ni after modification and a decrease in electron density around Ni, consistent with the XPS results. The orthogonal derivative of the K-edge absorption further reveals a higher absorption peak of Ni at 8346 eV in NFBF(6:2), validating an increase in the oxidation state of Ni and thus electron gain, consistent with the XPS results.

To analyze the bonding information, the extended XAFS (X-ray absorption fine structure) spectra were analyzed. As shown in Fig. 4(i), the EXAFS spectra exhibit a prominent Ni peak at approximately 1.55 Å, attributed to the first coordination shell of isolated Ni–O bonds [44]. Additionally, another peak at 2.10 Å is associated with the second coordination shell of Ni–Ni bonds. Wavelet transform (WT)-EXAFS analysis further identifies two characteristic regions of Ni–O and Ni–Ni scattering: the first shell domain exhibits a local maximum at R = 1.55 Å and k = 6.5 $Å^{-1}$, and the second shell domain exhibits a local maximum at R = 2.10 Å and k = 8.1 $Å^{-1}$ (Fig. 4(i)).

In this section, the successful synthesis of the NFBF(6:2) material was confirmed through a series of characterization techniques, which provided detailed insights into its nanoflower-like morphology, crystal structure, elemental distribution, chemical bonding states, and modifications to its electronic structure. The results indicate that NFBF(6:2) exhibits a well-defined crystal structure and chemical composition. Furthermore, the incorporation of the ferrocene ligand effectively modulated the electronic properties of the material.

2.4 The multi-environment adaptability of NFBF(6:2)

To validate the multi-environment adaptability of NFBF(6:2), we tested its electrocatalytic performance for water electrolysis OER under various conditions: standard alkaline environment (1 M KOH), urea electrolyte environment simulating urea concentration in human urine (1 M KOH + 0.33 M Urea), simulated seawater conditions (1 M KOH + 0.5 M NaCl, 1 M KOH + 1 M NaCl) (Fig. 5(f)).

Consistent with previous studies, we initially tested the LSV curves of NFBF(6:2) under various environments. In prior research [45], it was commonly observed that the electrocatalytic kinetics of the UOR process were superior to those of the OER process, owing to the significantly lower equilibrium potential of UOR (0.37 V vs. RHE) compared to OER (1.23 V). However, in our experiments, as depicted in Fig. 5(a), we observed that during the UOR reaction, the overpotential was initially lower compared to the OER reaction in the standard alkaline environment, up to a current density of about 70 $mA{\cdot}cm^{-2}$, after which the overpotential gradually increased, leading to a decline in electrocatalytic performance. During the urea electro-oxidation reaction, by-products and intermediates are gradually produced, among which the generated CO_2 dissolves in water. As the current density increases, the reaction rate accelerates, and the HCO_3^- formed from the CO_2 dissolved in water, along with some by-products, rapidly accumulate on the electrode surface, leading to electrode surface poisoning and increased overpotential.

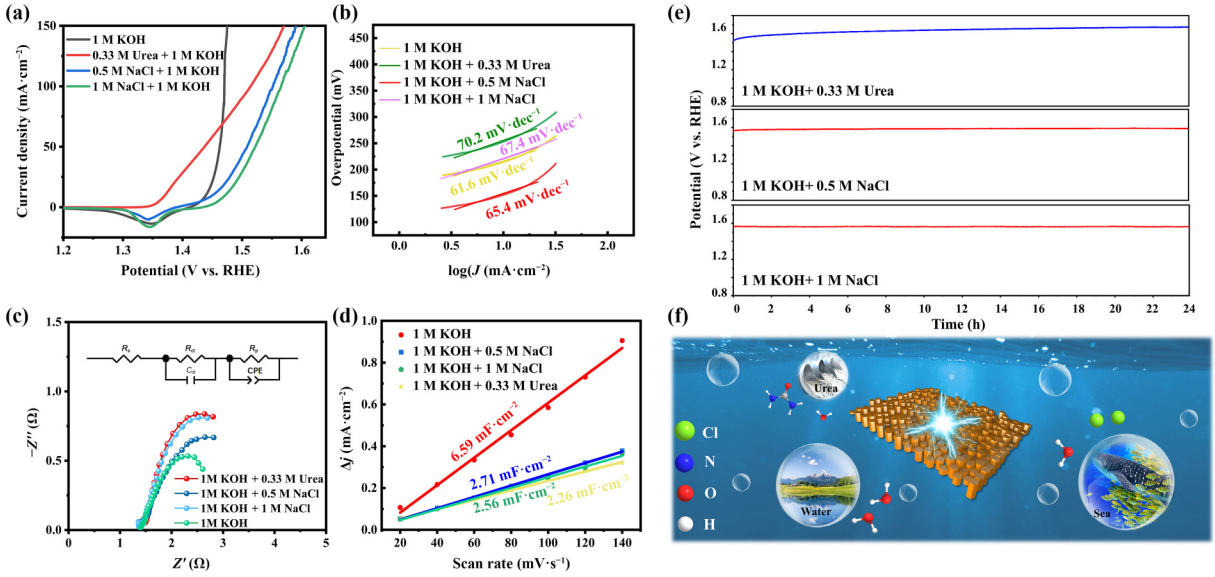

Figure 5 (a) LSV curves. (b) Tafel slope. (c) Nyquist plots. (d) Linear fitting of current density as a function of the scan rate. (e) Stability test performed at 50 mA·cm^{-2} of NFBF(6:2) in various electrolytes. (f) The adaptability across various environments of NFBF(6:2).

The N_2 produced forms a bubble layer at high current densities, which hinders the contact between the electrode and the electrolyte, thereby increasing the overpotential. At low current densities, the bubble generation rate is slower, allowing the bubbles to escape in a timely manner, which does not significantly affect the reaction on the electrode surface. Nonetheless, we also obtained results consistent with expectations: The LSV curves under the two simulated seawater environments exhibited slightly higher overpotentials compared to the standard alkaline environment, due to the varying degrees of interference from Cl^-. Moreover, as the concentration of Cl^- increased, there was a corresponding escalation in overpotential.

Besides, we also obtained Tafel curves for NFBF(6:2) under various environments. As shown in Fig. 5(b), the Tafel slope of the material in the standard alkaline environment (61.6 mV·dec^{-1}) was the smallest, while it was the highest in the urea environment (70.6 mV·dec^{-1}), consistent with the previous LSV results. The Tafel slopes in the two simulated seawater environments were 65.4 and 67.4 mV·dec^{-1}, respectively, in line with the expected outcomes. EIS results further corroborated the authenticity of the findings. The fitted EIS plots, as shown in Fig. 5(c), revealed that the impedance semicircle radius was the largest in the urea environment and smallest in the standard alkaline environment. In the two simulated seawater environments, the impedance semicircle radius decreased as the chloride ion concentration diminished. The precise parameters of the fitted circuit components were meticulously detailed in Table S3 in the ESM. Subsequently, to reaffirm the accuracy of our findings, we employed C_{dl} plots for validation. As depicted in Fig. 5(d) and Fig. S15 in the ESM, it becomes evident that the C_{dl} value exhibited a notable augmentation in the urea environment compared to alternative conditions, aligning impeccably with our previous assessments. The electrocatalytic stability and durability of NFBF(6:2) under multiple environments, as shown in Fig. 5(e) and Fig. S14 in the ESM, by comparison, we found that NFBF(6:2) not only maintains excellent stability in regular alkaline environments but also exhibits outstanding more than 100-hour stability in simulated seawater with two different chloride ion concentrations, which is beyond our expectations. Additionally, we observed that in a urea-containing environment, the overpotential of NFBF(6:2) tends to increase during the initial 20–70 h, the stability of NFBF(6:2) in a urea-containing environment deteriorates due to the aforementioned influences, providing a direction for subsequent material improvements. These observations indicate the superior electrocatalytic water-splitting performance and notable adaptability of NFBF(6:2) across various environments.

2.5 Overall water splitting adaptability of NFBF(6:2)

Based on the experimental results mentioned above, we aim to demonstrate that the NFBF series materials can exhibit excellent electrocatalytic prowess under real seawater conditions, similar to simulated seawater environments. Therefore, we first verified the electrocatalytic OER performance of the NFBF materials under alkaline seawater conditions.

In a three-electrode system, the performance of different NFBF materials with varying ratios was meticulously compared under alkaline seawater conditions. As shown in Fig. S22(a) in the ESM, in alkaline seawater environment, the overpotentials at a current density of 50 mA·cm^{-2} for NFBF(1:1), NFBF(5:3), NFBF(3:5), and NFBF(6:2) were 430, 415, 409, and 278 mV, respectively. Additionally, we compared the performance with the unmodified material NFB, which exhibited an overpotential of 465 mV under the same conditions. Consistently, NFBF(6:2) achieved the lowest overpotential, aligning with the previously observed adaptability across multiple environments. Furthermore, as depicted in Fig. S22(b) in the ESM, the Tafel slope for NFBF(6:2) was 83.4 mV·dec^{-1}, lower than that of the other samples. Additionally, Fig. S22(c) in the ESM indicates that NFBF(6:2) had the most diminutive semicircle diameter among all the compared materials, with EIS results harmonizing seamlessly with the overpotential and Tafel slope values. The electrochemic C_{dl} results (Figs. S24 and S22(d) in the ESM) revealed that both the unmodified (2.0 mF·cm^{-2}) and other ratio NFBF materials had lower C_{dl} values compared to NFBF(6:2) (3.4 mF·cm^{-2}). This discrepancy indicates a higher exposure of active metal sites on the surface of the electrocatalyst NFBF(6:2), thus substantiating the highest OER electrocatalytic activity.

Therefore, by selecting the best-performing NFBF(6:2) as both the anode and cathode components, we innovatively assembled a dual-electrode structure for the first time, with utilizing traditional 1 M KOH electrolyte and alkaline seawater electrolyte. As shown in Figs. S22(f), S22(j), and S22(k) in the ESM, under normal alkaline conditions, (+) NFBF(6:2) || NFBF(6:2) (−) arrangement demonstrated exceptional overall water splitting (OWS) performance, driving current densities of 10, 50, and 100 mA·cm^{-2} at low voltages of 1.40, 1.56, and 1.67 V, respectively, whereas (+) NF||NF (−) could provide the same current density at higher cell voltages of 1.65, 1.80, and 1.95 V. This groundbreaking performance surpasses many recently reported similar bifunctional electrocatalysts (Fig. S22(i) and Table S5 in the ESM).

Moreover, during overall seawater splitting, (+) NFBF(6:2) || NFBF(6:2) (−) necessitated merely 1.44, 1.64, and 1.80 V of cell voltage to deliver current densities of 10, 50, and 100 mA·cm^{-2}, respectively, while (+) NF||NF (−) counterpart could provide the same current density at 1.70, 2.10, and 2.50 V (Fig. S22(e) in the ESM). Compared to other reported catalysts, this bifunctional electrode remains competitively positioned (Fig. S22(h) and Table S4 in the ESM). Furthermore, the high stability of (+) NFBF(6:2) || NFBF(6:2) (−) in 1 M KOH electrolyte and alkaline seawater media was also conclusively confirmed through a rigorous more than 100-hour stability test (Fig. S22(g) in the ESM).

2.6 The electrocatalytic principle and DFT calculations

We further delve into the microstructure analysis of the optimal material NFBF(6:2) after the OER reaction using SEM and HRTEM. SEM images of NFBF(6:2) and NFB after 24 h of stability testing (Figs. 6(a) and 6(b), and Fig. S16 in the ESM) revealed that the morphology of both MOFs remained largely unaltered post-OER. The basic morphology persisted intact, with only the nanoflowers of NFBF(6:2) appearing slightly thinner, accompanied by slight curling and collapsing. It was observed that the modified NFBF(6:2) exhibited greater stability in terms of morphology preservation.

TEM image (Fig. 6(c)) offered a detailed glimpse into the structural alterations of NFBF(6:2) retained their nanoflower morphology, albeit with thinner layers, indicating a subtle evolution in structure under the catalytic conditions. Additionally, HRTEM analysis (Fig. 6(d)) provided deeper insights, showing lattice spacings consistent with the actual values. Specifically, a lattice spacing of 0.26 nm corresponded to the (101) crystal plane of Ni $(OH)_2$ [38], while a spacing of 0.21 nm corresponded to the (111) crystal plane of NiOOH, confirming the partial formation of Ni^{II}-OH(byproduct) and Ni^{III}-OOH on NFBF(6:2) after the OER catalysis, as expected. EDS results confirmed the homogeneous distribution of C, O, Fe, and Ni elements within NFBF(6:2) (Fig. 6(e)).

To investigate the structural and morphological changes of NFBF(6:2) during the OER process, we conducted XRD, FTIR, and Raman tests on NFBF(6:2) after 24 h of stability testing. The XRD analysis in Fig. S23(a) in the ESM reveals the structural changes of NFBF(6:2) before and after OER. By comparing characteristic peaks, it was observed that post-OER NFBF(6:2) retained some MOF characteristic peaks, yet some peaks matched those of NiOOH (PDF#00-006-0075) and Ni $(OH)_2$ (PDF#00-001-1047), indicating structural changes in the MOF after OER [25], with partial transformation into NiOOH and Ni $(OH)_2$, consistent with TEM data. FTIR spectra demonstrated changes in chemical bonds of NFBF(6:2) pre- and post-OER [29].

As shown in Fig. S23(b) in the ESM, although the carboxyl characteristic peaks at 1400–1680 cm^{-1} were partially preserved, they exhibited broader and weaker peaks. Additionally, significant changes were observed in the aromatic ring characteristic peaks at 1000–1300 cm^{-1}, manifesting as the appearance of inverse peaks. These observations suggest diminished sample crystallinity and

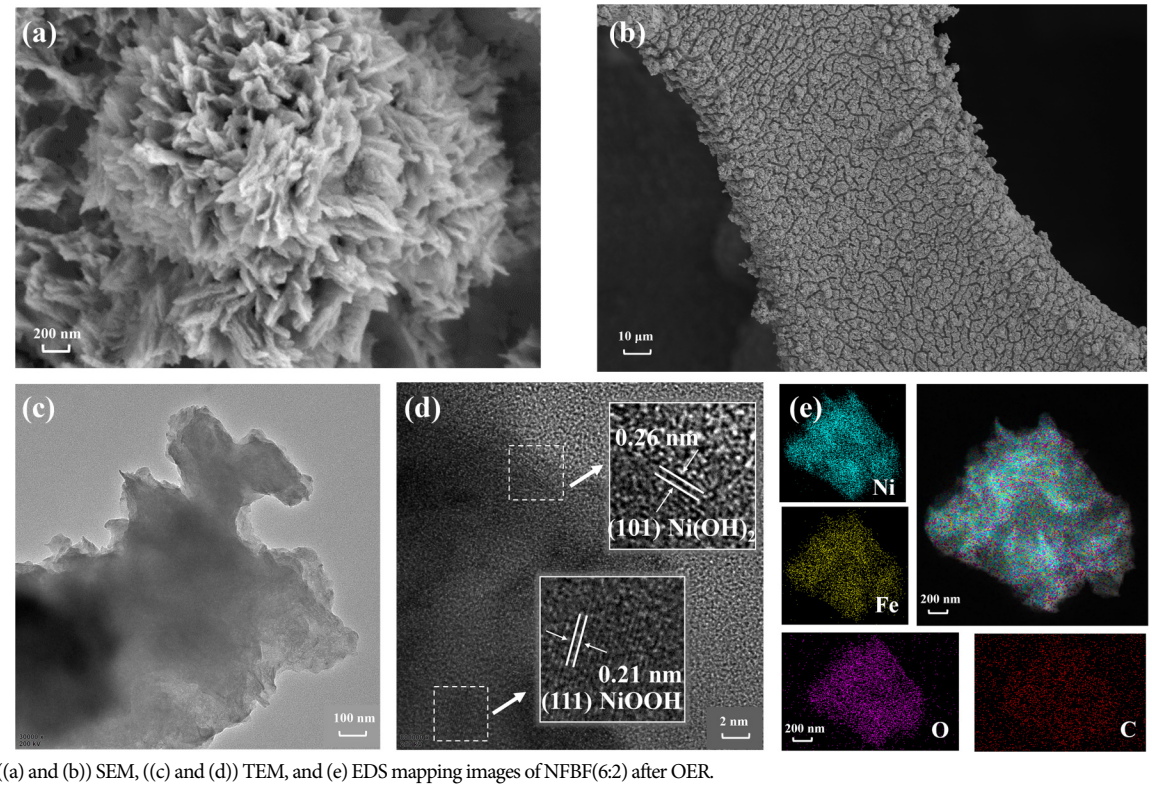

Figure 6 ((a) and (b)) SEM, ((c) and (d)) TEM, and (e) EDS mapping images of NFBF(6:2) after OER.

lend further credence to the structural modifications within the MOF, as inferred from the FTIR spectra. Particularly striking was the M–O bond characteristic peaks within the range of 400–600 cm^{-1}, indicating the generation of abundant NiOOH. These results were corroborated by Raman spectroscopy (Fig. S23(c) in the ESM) [29], where the pre-reaction NFBF(6:2) is represented by black curve. The characteristic peaks of Fc at 342 and 609 cm^{-1}, M–O at 412 and 518 cm^{-1}, aromatic rings at 865, 1139, and 1422 cm^{-1}, and –COO– at 1612 cm^{-1} were observed. After OER, the aromatic ring and organic ligand characteristic peaks disappeared, leaving behind only Ni^{II}–O (480, 550 cm^{-1}), Ni^{III}–OO– (~ 1150 cm^{-1}), and metal bonds in Fc ligands (296 cm^{-1}). These observations strongly indicate structural transformations in the MOF, consistent with the XRD results.

To explore the changes in oxidation states of elements during the OER process, XPS analysis was performed on NFBF(6:2) after 24 h of *i*–*t* testing. The full XPS survey spectra (FXPS) results clearly demonstrate, as illustrated in Fig. S25 in the ESM, that Ni, Fe, C, and O elements are present in both NFB and NFBF(6:2) after the electrocatalytic OER reaction, indicating that the electrocatalytic process does not affect the elemental composition. Post-OER high-resolution XPS spectra of Ni 2p (Fig. S23(d) in the ESM) exhibited four main peaks associated with Ni^{2+} $2p_{3/2}$, Ni^{2+} $2p_{1/2}$, Ni^{3+} $2p_{3/2}$, and Ni^{3+} $2p_{1/2}$ orbitals, with binding energies of 856.1, 873.7, 858.7, and 876.6 eV, respectively, indicating partial oxidation of MOFs to Ni^{III}-OOH during OER. Similarly, the high-resolution XPS spectra of Fe 2p after OER (Fig. S23(e) in the ESM) showed characteristic peaks corresponding to Fe^{3+} and Fe^{2+} at 712.3, 724.9, 710.0, and 721.5 eV, respectively, signaling no alteration in Fe oxidation state post-reaction. The same characteristics were observed in different electrolyte environments (Fig. S23(g) in the ESM), confirming consistent changes in characteristic peaks pre- and post-OER across various conditions. Detailed XPS peak data can be found in Table S6 in the ESM.

Operando Raman optical microscopy spectra of NFBF(6:2) captured in various reaction environments (1.1–1.6 V vs. RHE) further elucidate this point. In a 1 M KOH solution, we observed that at the open circuit potential (OCP) of 0.24 V and below, most of the Ni exist in the +2-oxidation state, as evidenced by Raman characteristic peaks at 467 and 527 cm^{-1}, representing the Ni^{II}–O band, with low intensity (Fig. 7(a)). After reaching the open circuit potential, Ni transitions to the +3-oxidation state, with Raman

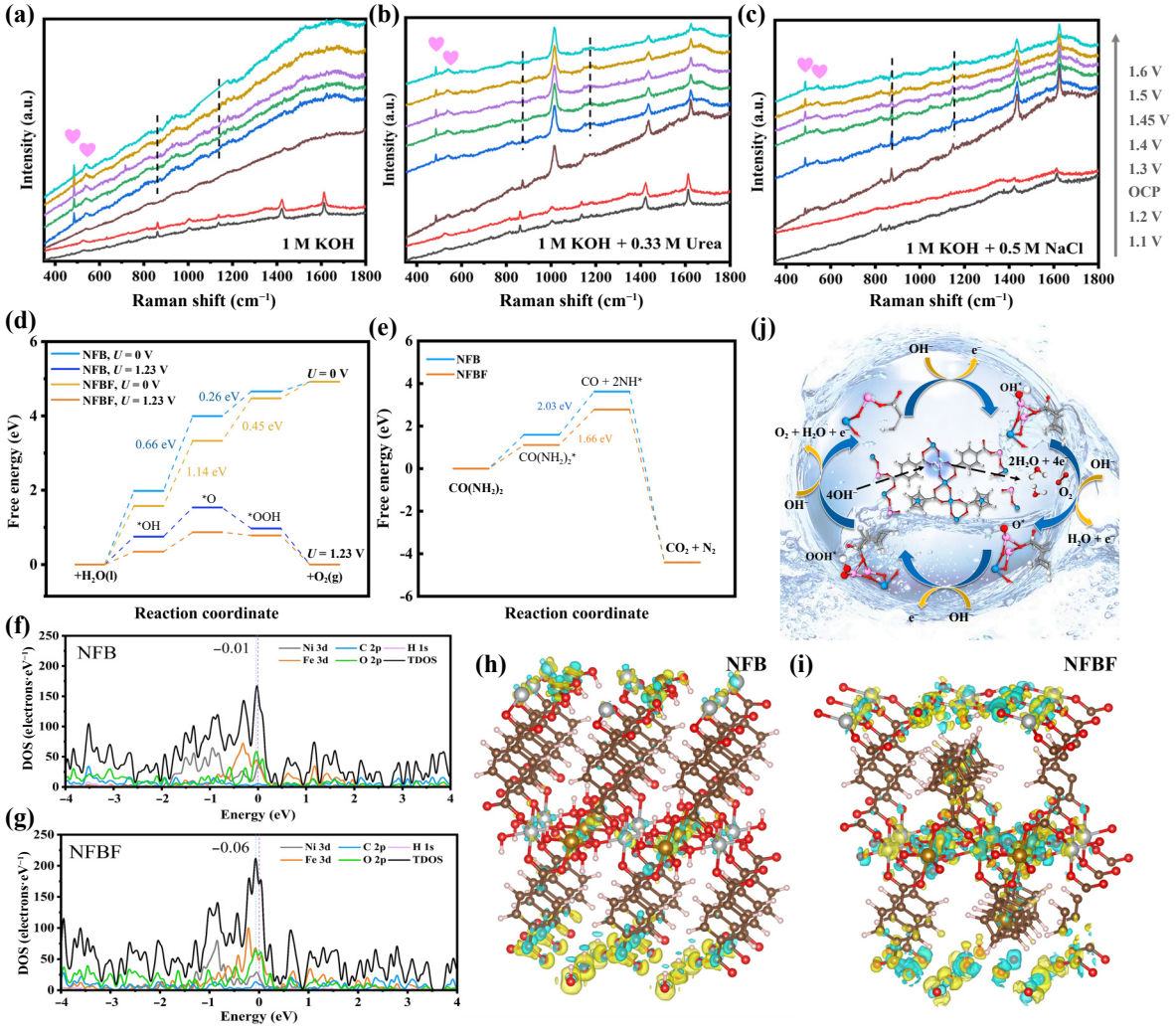

Figure 7 *In-situ* Raman spectroscopy of NFBF during OER in (a) 1 M KOH, (b) 1 M KOH + 0.33 M Urea and (c) 1 M KOH + 0.5 M NaCl. (d) Free energy diagram for OER and (e) UOR on NFB and NFBF. (f) and (g) TDOS and PDOS diagrams of NFB and NFBF. Difference charge density of (h) NFB and (i) NFBF. The dark yellow, grey, brown, red, and white balls represent Ni, Fe, C, O, and H atoms, respectively. Blue and yellow represent electron depletion and electron accumulation with the isosurface value of 0.02 e·$Bohr^{-3}$, respectively. (j) Proposed OER mechanisms of NFBF.

characteristic peaks at 483 and 551 cm^{-1} representing the Ni^{III}–OOH band, which exhibit high intensity. Characteristic peaks observed in the wavenumber range of 850–1150 cm^{-1} are attributed to superoxide species O–O– [45], and it can be observed that with increasing potential, the Raman characteristic peaks of O–O– show a trend of increasing intensity, indicating an increase in the quantity of active oxygen. In a 1 M KOH + 0.33 M Urea solution, as shown in Fig. 7(b), we found that the change in Raman characteristic peaks follows a pattern consistent with that observed in the 1 M KOH solution, except for the appearance of symmetric C–N stretching of urea at 1004 cm^{-1} [46]. Similarly, in a 1 M KOH + 0.5 M NaCl solution (Fig. 7(c)), *operando* Raman optical microscopy revealed the same pattern of characteristic peak changes.

Based on these results, we delineated the charge transfer process and electron interactions of NFBF(6:2) from the perspective of the valence electronic structure (Fig. 8) [47]. On the π-symmetric (t_{2g}) d orbitals, Fe^{3+} ($t_{2g}^3e_g^2$) exhibited a high-spin valence electronic configuration with three unpaired electrons, resulting in weak electron interactions that could attract electrons, while Ni^{2+} ($t_{2g}^6e_g^2$) had a fully occupied π-symmetric (t_{2g}) d orbital, leading to strong electron interactions and electron repulsion. Additionally, the Fe atoms of the Fc ligands could lose electrons, potentially leading to increased oxidation states [38].

Consequently, we proposed the reaction mechanism of the NFBF(6:2) electrocatalyst: Ni acted as the active site, wherein coupling with Fe initiates partial electron transfer occurred from Ni^{2+} to Fe^{3+}. Moreover, the electron affinity of the Fc ligand promotes some electron transfer, which effectively regulates the electron configuration of Ni sites (matching XPS analysis results) and optimizes the bond strength between Ni sites and adsorbed oxygen. With decreasing electron density, the partially filled e_g orbitals of Ni^{2+} are primed to form appropriate bonds with adsorbed oxygen, promoting catalytic activity and hastening the reaction rate.

We also use DFT calculations in order to prove the above mechanism and the reason for the improvement before and after modification. The calculations were performed using the Vienna *ab initio* simulation package (VASP), with the Perdew–Burke–Ernzerhof (PBE) functional employed to describe electron interactions. Bader charge analysis was utilized to quantify charge transfer, while spin polarization was incorporated to account for interactions between orbitals. The resulting free energy diagram for adsorption was obtained based on these calculations. The commonly used computational model in current research was employed for calculations, which aligned well with the experimental data [48]. Figure S17 in the ESM shows NFB and NFBF structures. To shed light on the influence of modification on the electronic structure of NFB, the differential charge density simulations for NFBF and NFB were conducted. As shown in Fig. 7(h), many electrons accumulate around the organic ligands BDC and FcDA, while a decrease in charge occurs around the Ni atoms. This suggests a modulation of the electronic structure at the metal center upon Fc ligand incorporation, consistent with the previous XPS and XANES results. To uncover the source of their catalytic activity, the density of states (DOS) calculations were performed.

As depicted in Fig. 7(f), it is observed that more electrons are located near the Fermi level (dashed line) of NFBF, implying better conductivity. This anticipated electron transfer and redistribution can significantly reduce the reaction energy barrier, accelerate the catalytic process, thermodynamically enhance the catalyst's affinity for oxygen intermediates, thus fortifying the adsorption of the electrocatalyst. To further reveal the excellent catalytic activity of these catalysts, the free energy differences (ΔG) for each elementary step were calculated to estimate OER (Fig. 7(d)). The intermediate model diagrams required for the calculations are shown in Figs. S18 and S19 in the ESM. From the computational results, it is inferred that at U = 1.23 V, by estimating the ΔG of each reaction pathway, the step with the largest ΔG (0.66 eV) for NFBF conversion to O* is the potential-determining step, whereas although the RDS of NFB is the same as that of NFBF, its respective ΔG is 1.14 eV, indicating

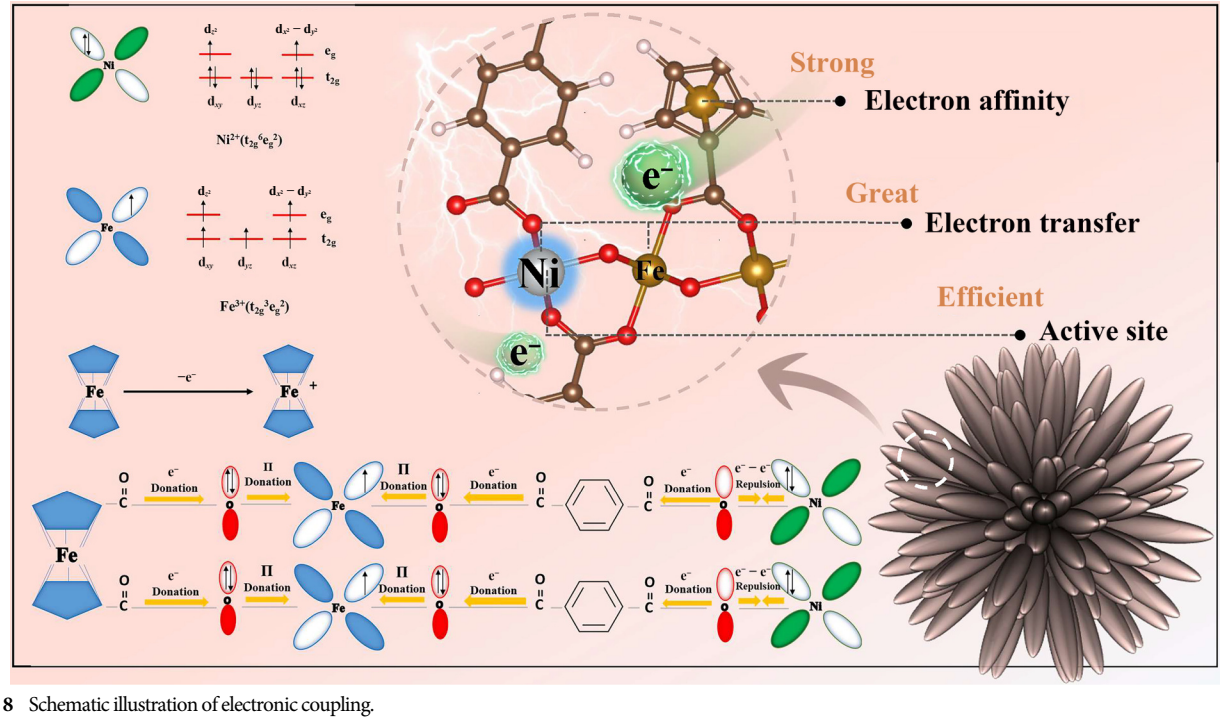

Figure 8 Schematic illustration of electronic coupling.

that the reaction overpotential of NFBF is lower and synergistically contributes to OER activity. This disparity underscores the anticipated NFBF exhibits superior OER performance. Finally, to further describe the catalytic UOR activity at Ni sites, the reaction barriers for UOR on the NFB and NFBF surfaces were computed. This analysis encompassed the adsorption of $CO(NH_2)_2$ and subsequent conversion of $CO(NH_2)_2$* to NH* and CO* as intermediate products (i.e., the RDS).

The atomic structures of reaction intermediates ($CO(NH_2)_2$*, NH*, and CO*) on NFB and NFBF are depicted in Figs. S20 and S21 in the ESM. Specifically, in Fig. 7(g), the necessary adsorption energy for $CO(NH_2)_2$ at the Ni sites in NFB amounts to 2.03 eV. Conversely, the corresponding energy for NFBF is notably reduced to 1.66 eV, indicating a lowered adsorption energy barrier of $CO(NH_2)_2$ at the Ni sites in NFBF compared to NFB. This suggests that the modification effectively facilitates the acceleration of UOR kinetics.

3 Conclusions

In summary, we have designed a novel MOF material, NFBF(6:2). Through extensively comprehensive characterization of its lattice structure and electrochemical performance testing, we discovered that the needle-like nanoflower structure of the double-metal double-ligand NFBF(6:2) exhibits optimal electrocatalytic performance at 10 $mA{\cdot}cm^{-2}$ (210 mV), and we have elucidated the underlying regulatory principles governing the structure and performance of analogous MOF materials. Characterization experiments such as *operando* Raman spectroscopy and XAFS unveiled electronic restructuring dynamics during the catalytic OER process. DFT calculations showed that NFBF(6:2) possesses an optimized electronic structure, with lower reaction energy barriers compared to the original NFB phase. Notably, the electron-rich ferrocene groups in NFBF(6:2) facilitate electron transfer during both the OER and UOR electrocatalysis process, reducing the free energy of adsorbed intermediates and accelerating the electrocatalytic reaction. Remarkably, in the complete water-splitting system, (+) NFBF(6:2) || NFBF(6:2) (−) exhibits impressive performance in alkaline freshwater and seawater electrolyzers. Overall, this work not only highlights the importance of designing and synthesizing MOFs for promoting OER catalysts, but also facilitates the development of efficient OER catalysts for the understanding of morphology–function relationships in multienvironment water splitting reaction.

4 Methods

4.1 Regents and materials

$NiCl_2{\cdot}6H_2O$, terephthalic acid, and potassium hydroxide were provided by Tianjin Heowns Biochemical Technology Co., Ltd (China). $FeCl_3{\cdot}6H_2O$ and FcDA were provided by Shanghai Titan Scientific Co., Ltd (China). Urea was provided by Tianjin Zhiyuan Reagent Co., Ltd (China). Sea salt was purchased online. All reagents were used directly without further purification.

4.2 Sample preparation

Synthesis of M-BDC (M = Ni, Fe). Commercial NF (1 cm × 2 cm) was rinsed three times with HCl aqueous solution (3 M), absolute alcohol, and DI water with the assistance of sonication. In a typical synthesis of Ni-MOF, 0.8 mmol of $NiCl_2{\cdot}6H_2O$ ($FeCl_3{\cdot}6H_2O$) and 0.8 mmol of H_2BDC were successively dissolved in a mixed solvent of 28 mL DMF, 4 mL ethanol, and 4 mL DI water under continuous ultrasonic conditions. Afterward, the solution and a piece of clean NF were transferred into a Teflon vessel which was placed upright in electric oven and maintained at 125 °C for 12 h. When cooling down to room temperature, the NF was taken out, rinsed with DI water, and dried for future use.

Synthesis of M-Fc (M = Ni, Fe). Similar to the method of synthesizing M-BDC, but with changes that 0.8 mmol of $NiCl_2{\cdot}6H_2O$ ($FeCl_3{\cdot}6H_2O$) and 0.8 mmol of FcDA were added in the mixed solvent, other methods were the same.

Synthesis of M-BDC/Fc (M = Ni, Fe). Similar to the method of synthesizing M-BDC, but with changes that 0.8 mmol of $NiCl_2{\cdot}6H_2O$ ($FeCl_3{\cdot}6H_2O$), and a series of proportions (1:1, 6:2, 5:3, 3:5) of H_2BDC and FcDA were added in the mixed solvent, other methods were the same.

Synthesis of NiFe-BDC. Similar to the method of synthesizing M-BDC, but with changes that 0.56 mmol of $NiCl_2{\cdot}6H_2O$, 0.24 mmol $FeCl_3{\cdot}6H_2O$, and 0.8 mmol of H_2BDC were added in the mixed solvent, other methods were the same.

Synthesis of *n*:*m* NFBF (1:1, 6:2, 5:3, and 3:5). Similar to the method of synthesizing NiFe-BDC, but with changes that 0.56 mmol of $NiCl_2{\cdot}6H_2O$, 0.24 mmol $FeCl_3{\cdot}6H_2O$, and a series of proportions (1:1, 6:2, 5:3, and 3:5) of H_2BDC and FcDA were added in the mixed solvent, other methods were the same.

Preparation of RuO_2/NF. The preparation of RuO_2/NF electrode: the mixture of RuO_2 (10 mg), Nafion solution (30 μL), and ethanol (470 μL) was ultrasonicated for 30 min. A piece of NF (1.0 cm × 1.0 cm) was coated with 50 μL of the dispersion, which was then allowed to dry for 2 h at room temperature.

4.3 Characterization

XRD patterns of all the samples were obtained using a Rigaku X-ray diffractometer (Ultima IV) equipped with Cu-Kα radiation (40 kV, 20 mA). For the XRD analysis, an appropriate amount of the catalytic material grown on nickel foam was scraped off and ground into a fine powder to ensure uniformity. The resulting XRD patterns confirmed that the characteristic peaks of the Ni substrate did not interfere with the interpretation of the results. XPS analysis was conducted using the Thermo Scientific ESCALAB Xi+ X-ray photoelectron spectrometer. The morphological structures of the samples were investigated using a field emission scanning electron microscope (ZEISS GeminiSEM 300) and a TEM (Talos F200S). FT-IR spectra were recorded on IRTracer-100 (Shimadzu) at room temperature. Raman spectra were acquired on a DXR2xi (Thermo) Raman microscope.

4.4 Electrochemical measurements

The OER measurements were investigated at room temperature in 1.0 M KOH aqueous solution using an electrochemical workstation (DH7000, Donghua, Jiangsu, China) with a standard three-electrode system. The synthetic sample was used as the working electrode (1 cm × 1 cm), a Hg/HgO as the reference electrode, and graphite rod as the counter electrode.

All of the electrochemical tests were conducted with different electrolytes (1 M KOH, 1 M KOH + 0.33 M Urea, 1 M KOH + 0.5 M NaCl, 1 M KOH + 1 M NaCl, 1 M KOH + seawater). The seawater was obtained by diluting sea salt with distilled water.

To obtain stable current densities, the working electrode was activated by 50 cycles of CV before the LSV measurements.

Thereafter, all OER polarization curves with a scan rate of 5.0 mV·s^{-1} were measured to reduce capacitor current effect. According to the Eq. (1)

$$E_{RHE} = E_{Hg/HgO} + 0.098 + 0.059\text{pH V} \quad (1)$$

All potentials were calibrated as RHE. The overpotential (η) was calculated by the Eq. (2)

$$\eta = E_{RHE} - 1.23\text{ V} \quad (2)$$

The Tafel slope was calculated by the Eq. (3)

$$E_{RHE} = a + b \times \log j \quad (3)$$

where b refers to the Tafel slope, j represents the current density. All EIS were obtained in the range from 100 kHz to 0.01 Hz and the chronopotentiometry was measured using an electrochemical workstation system. All the LSV curves were manually corrected with 90% iR compensation. The ECSA of the catalysts was calculated by the C_{dl} method. The CV measurements were performed in non-Faradaic region (1.1 to 1.25 V vs. RHE) at different scan rates of 20, 40, 60, 80, 100, 120, and 140 mV·s^{-1}. C_{dl} value was estimated by plotting the $\Delta J = (Ja - Jc)/2$ against the scan rate. The linear slope was equivalent to the C_{dl}. The durability tests were carried out at fixed current densities of 100 and 500 mA·cm^{-2} using the chronopotentiometry technique.

The overall water splitting tests were conducted in a three-electrode electrolytic cell using both alkaline electrolyte (1 M KOH) and alkaline seawater electrolyte (seawater + 1 M KOH). The working electrode and counter electrode were both NFBF(6:2), while the reference electrode was Hg/HgO. The overall water splitting system was denoted as NFBF(6:2) || NFBF(6:2).

4.5 Computational details

All the calculations were performed in the framework of the density functional theory with the projector augmented plane-wave method, as implemented in the Vienna *ab initio* simulation package. The generalized gradient approximation proposed by PBE was selected for the exchange-correlation potential. The cut-off energy for plane wave was set to 480 eV. The energy criterion was set to 10^{-5} eV in the iterative solution of the Kohn–Sham equation. All the structures were relaxed until the residual forces on the atoms had declined to less than 0.02 eV·Å^{-1}. To avoid interlaminar interactions, a vacuum spacing of 20 Å was applied perpendicular to the slab.

Here, we define $\Delta\rho = \rho_{A+B} - \rho_A - \rho_B$ as the charge density difference of A/B heterostructure, where $\rho_{A/B}$, ρ_A, and ρ_B are the charge densities of A/B heterostructure, isolated A and B slabs, respectively.

We use the Bader charge to express the charge transfer quantity.

Here, differences in Gibbs free energy (ΔG) for intermediates defined as Eq. (4)

$$\Delta G = \Delta E + \Delta E_{ZPE} - T\Delta S + \Delta G_U \quad (4)$$

where ΔG is the total energy difference between the slab and respective terminations computed by DFT–PBE. ΔE_{ZPE} and $T\Delta S$ denote differences in zero-point energy and entropy between adsorbed states of reaction intermediates and gap phase, respectively. T is the room temperature (298.15 K). $\Delta G_U = -eU$, whereby U is the electrode potential.

Electronic Supplementary Material: Supplementary material (overpotential comparison, Tafel curve, XRD patterns of a series of MOF materials, the calculation model and free energy diagram for OER on NFB and NFBF, etc.) is available in the online version of this article at https://doi.org/10.26599/NR.2025.94907305.

Data availability

All data needed to support the conclusions in the paper are presented in the manuscript and the Electronic Supplementary Material. Additional data related to this paper may be requested from the corresponding author upon request.

Acknowledgements

We acknowledge financial support from the National Natural Science Foundation of China (No. 21401151), Fundamental Research Funds for the Central Universities (No. 2682023ZTPY064), and Sichuan Provincial Administration of Traditional Chinese Medicine Project (No. 2023MS212).

Declaration of competing interest

The authors declare that they have no known competing financial interests or personal relationships that could have appeared to influence the work reported in this paper.

Author contribution statement

S. Y. F.: Data curation, project administration, validation, writing manuscript, experimental design. X. P. H., L. L., Y. X., W. Y. G., and Z. G.: Data curation, project administration, validation, experimental design. C. J. W.: Project administration, funding acquisition. All the authors have approved the final manuscript.

Use of AI statement

None.

References

[1] Chu, S.; Majumdar, A. Opportunities and challenges for a sustainable energy future. *Nature* **2012**, *488*, 294–303.

[2] Zhang, Y.; Mu, X. Q.; Liu, Z. Y.; Zhao, H. Y.; Zhuang, Z. C.; Zhang, Y. F.; Mu, S. C.; Liu, S. L.; Wang, D. S.; Dai, Z. H. Twin-distortion modulated ultra-low coordination PtRuNi-O_x catalyst for enhanced hydrogen production from chemical wastewater. *Nat. Commun.* **2024**, *15*, 10149.

[3] Dawood, F.; Anda, M.; Shafiullah, G. M. Hydrogen production for energy: An overview. *Int. J. Hydrogen Energy* **2020**, *45*, 3847–3869.

[4] Chen, F. J.; Mu, X. Q.; Zhou, J. L.; Wang, S. C.; Liu, Z. Y.; Zhou, D. Y.; Liu, S. L.; Wang, D. S.; Dai, Z. H. Engineering the active sites of MOF-derived catalysts: From oxygen activation to activate metal-air batteries. *Chin. J. Chem.* **2024**, *42*, 2520–2535.

[5] Ji, Z. J.; Song, Y. J.; Zhao, S. H.; Li, Y.; Liu, J.; Hu, W. P. Pathway manipulation via Ni, Co, and V ternary synergism to realize high efficiency for urea electrocatalytic oxidation. *ACS Catal.* **2022**, *12*, 569–579.

[6] Mu, X. Q.; Yu, M.; Liu, X. Y.; Liao, Y. R.; Chen, F. J.; Pan, H. Z.; Chen, Z. Y.; Liu, S. L.; Wang, D. S.; Mu, S. C. High-entropy ultrathin amorphous metal-organic framework-stabilized Ru(Mo) dual-atom sites for water oxidation. *ACS Energy Lett.* **2024**, *9*, 5763–5770.

[7] Ye, K.; Wang, G.; Cao, D. X.; Wang, G. X. Recent advances in the

electro-oxidation of urea for direct urea fuel cell and urea electrolysis. *Top. Curr. Chem. (Cham)* **2018**, *376*, 42.

[8] Wang, L. G.; Wu, J. B.; Wang, S. W.; Liu, H.; Wang, Y.; Wang, D. S. The reformation of catalyst: From a trial-and-error synthesis to rational design. *Nano Res.* **2024**, *17*, 3261–3301.

[9] Wang, L. G.; Li, J. L.; Ji, S. F.; Xiong, Y. L.; Wang, D. S. Microenvironment engineering of covalent organic framework based single/dual-atom catalysts toward sustainable energy conversion and storage. *Energy Environ. Sci.* **2024**, *17*, 8482–8528.

[10] Tang, H. T.; Zhou, H. Y.; Pan, Y. M.; Zhang, J. L.; Cui, F. H.; Li, W. H.; Wang, D. S. Single-atom manganese-catalyzed oxygen evolution drives the electrochemical oxidation of Silane to Silanol. *Angew. Chem., Int. Ed.* **2024**, *63*, e202315032.

[11] Wang, L. G.; Su, H.; Tan, G. Y.; Xin, J. J.; Wang, X. G.; Zhang, Z.; Li, Y. P.; Qiu, Y.; Li, X. H.; Li, H. S. et al. Boosting efficient and sustainable alkaline water oxidation on a W-CoOOH-TT pair-sites catalyst synthesized via topochemical transformation. *Adv. Mater.* **2024**, *36*, 2302642.

[12] Meng, S. Y.; Li, G.; Wang, P.; He, M.; Sun, X. H.; Li, Z. X. Rare earth-based MOFs for photo/electrocatalysis. *Mater. Chem. Front.* **2023**, *7*, 806–827.

[13] Gao, Y.; Yang, C. D.; Sun, F. L.; He, D. P.; Wang, X. Q.; Chen, J.; Zheng, X. B.; Liu, R. C.; Pan, H. G.; Wang, D. S. Ligand-tuning metallic sites in molecular complexes for efficient water oxidation. *Angew. Chem., Int. Ed.* **2025**, *64*, e202415755.

[14] Wu, Q.; Gao, Q. P.; Shan, B.; Wang, W. Z.; Qi, Y. P.; Tai, X. S.; Wang, X.; Zheng, D. D.; Yan, H.; Ying, B. W. et al. Recent advances in self-supported transition-metal-based electrocatalysts for seawater oxidation. *Acta Phys.-Chim. Sin.* **2023**, *39*, 2303012.

[15] Wang, L. G.; Su, H.; Zhang, Z.; Xin, J. J.; Liu, H.; Wang, X. G.; Yang, C. Y.; Liang, X.; Wang, S. W.; Liu, H. et al. Co-Co dinuclear active sites dispersed on zirconium-doped heterostructured Co_9S_8/Co_3O_4 for high-current-density and durable acidic oxygen evolution. *Angew. Chem., Int. Ed.* **2023**, *62*, e202314185.

[16] Zheng, X. B.; Yang, J. R.; Li, P.; Wang, Q. S.; Wu,J. B.; Zhang, E. H.; Chen, S. H.; Zhuang, Z. C.; Lai, W. H.; Dou, S. X. et al. Ir-Sn pair-site triggers key oxygen radical intermediate for efficient acidic water oxidation. *Sci. Adv.* **2023**, *9*, eadi8025.

[17] Zheng, X. B.; Yang, J. R.; Xu, X.; Dou, S. X.; Sun, W. P.; Wang, D. S.; Wang, G. X. Deciphering cationic and anionic overoxidation: Key insights into the intrinsic structural degradation of catalysts. *Adv. Energy Mater.* **2024**, *14*, 2401227.

[18] Gan, T.; Wang, D. S. Atomically dispersed materials: Ideal catalysts in atomic era. *Nano Res.* **2024**, *17*, 18–38.

[19] Wang, Y.; Ma, F. Y.; Zhang, G. Q.; Zhang, J. W.; Zhao, H.; Dong, Y. M.; Wang, D. S. Precise synthesis of dual atom sites for electrocatalysis. *Nano Res.* **2024**, *17*, 9397–9427.

[20] Zheng, X. B.; Yang, J. R.; Li, P.; Jiang, Z. L.; Zhu, P.; Wang, Q. S.; Wu, J. B.; Zhang, E. H.; Sun, W. P.; Dou, S. X. et al. Dual-atom support boosts nickel-catalyzed urea electrooxidation. *Angew. Chem., Int. Ed.* **2023**, *62*, e202217449.

[21] Furukawa, H.; Cordova, K. E.; O'Keeffe, M.; Yaghi, O. M. The chemistry and applications of metal-organic frameworks. *Science* **2013**, *341*, 1230444.

[22] Xu, X. F.; Deng, Q. M.; Chen, H. C.; Humayun, M.; Duan, D. L.; Zhang, X; Sun, H. C.; Ao, X.; Xue, X. Y.; Nikiforov, A. et al. Metal-organic frameworks offering tunable binary active sites toward highly efficient urea oxidation electrolysis. *Research* **2022**, *2022*, 9837109.

[23] Zhang, K.; Liu, C. L.; Graham, N.; Zhang, G.; Yu, W. Z. Modulation of dual centers on cobalt-molybdenum oxides featuring synergistic effect of intermediate activation and radical mediator for electrocatalytic urea splitting. *Nano Energy* **2021**, *87*, 106217.

[24] Cai, M. M.; Zhu, Q.; Wang, X. Y.; Shao, Z. Y.; Yao, L.; Zeng, H.; Wu, X. F.; Chen, J.; Huang, K. K.; Feng, S. H. Formation and stabilization of NiOOH by introducing α-FeOOH in LDH: Composite electrocatalyst for oxygen evolution and urea oxidation reactions. *Adv. Mater.* **2023**, *35*, 2209338.

[25] Liu, D. M.; Xu, H.; Wang, C.; Ye, C. Q.; Yu, R.; Du, Y. K. *In situ* etch engineering of Ru doped $NiFe(OH)_x$/NiFe-MOF nanocomposites for boosting the oxygen evolution reaction. *J. Mater. Chem. A* **2021**, *9*, 24670–24676.

[26] Zhang, Y.; Shen, X. P.; Song, C. S.; Ji, Z. Y.; Du, F. H. Sulfur-doped $NiFe(CN)_5NO$ nanoparticles as efficient electrocatalysts for the oxygen evolution reaction. *J. Mater. Chem. A* **2023**, *11*, 8904–8911.

[27] Hu, J. S.; Xu, Q. L.; Wang, X. Y.; Huang, X. H.; Zhou, C. H.; Ye, Y.; Zhang, L.; Pang, H. Charge-transfer-regulated bimetal ferrocene-based organic frameworks for promoting electrocatalytic oxygen evolution. *Carbon Energy* **2023**, *5*, e315.

[28] He, F.; Zhao, Y. J.; Yang, X. X.; Zheng, S. X.; Yang, B.; Li, Z. J.; Kuang, Y. B.; Zhang, Q. H.; Lei, L. C.; Qiu, M. et al. Metal-organic frameworks with assembled bifunctional microreactor for charge modulation and strain generation toward enhanced oxygen electrocatalysis. *ACS Nano* **2022**, *16*, 9523–9534.

[29] Liu, J. Z.; Yang, J. F.; Song, Y. Y.; Sun, J. W.; Tian, Y. W.; Chen, Q.; Zhang, X. Y.; Zhang, L. X. Introducing non-bridging ligand in metal-organic framework-based electrocatalyst enabling reinforced oxygen evolution in seawater. *J. Colloid Interface Sci.* **2023**, *643*, 17–25.

[30] Li, P.; Li, W. Q.; Huang, Y. Q.; Huang, Q. H.; Tian, S. H. 3D hierarchical-architectured nanoarray electrode for boosted and sustained urea electro-oxidation. *Small* **2023**, *19*, 2300725

[31] Feng, S. W.; Fan, S. Y.; Li, L.; Sun, Z. Y.; Tang, H. W.; Xu, Y.; Fang, L.; Wang, C. J. Using hollow dodecahedral NiCo-LDH with multi-active sites to modify $BiVO_4$ photoanode facilitates the photoelectrochemical water splitting performance. *Nano Res. Energy* **2024**, *3*, e9120117.

[32] Tang, H. W.; Sun, Z. Y.; Fan, S. Y.; Feng, S. W.; Li, L.; Fang, L.; Wang, C. J. Fe-doped CoNi layered hydrogencarbonate hierarchical nano-array assisted growth of ZIF-67 as an efficient OER/UOR bifunctional catalyst reaction for overall urea-water electrolysis. *Chem. Eng. J.* **2024**, *491*, 152023.

[33] Wang, Z.; Xu, J.; Yang, J. H.; Xue, Y. H.; Dai, L. M. Ultraviolet/ozone treatment for boosting OER activity of MOF nanoneedle arrays. *Chem. Eng. J.* **2022**, *427*, 131498.

[34] Zhang, X.; Luo, J. S.; Wan, K.; Plessers, D.; Sels, B.; Song, J. X.; Chen. L. G.; Zhang, T.; Tang, P. Y.; Morante, J. R. et al. From rational design of a new bimetallic MOF family with tunable linkers to OER catalysts. *J. Mater. Chem. A* **2019**, *7*, 1616–1628.

[35] Bian, Q. N.; Guo, B. S.; Tan, D. X.; Zhang, D.; Kong, W. Q.; Wang, C. B.; Feng, Y. Y. Constructing CoNi-LDH/Fe MOF/NF heterostructure catalyst for energy-efficient OER and UOR at high current density. *ACS Appl. Mater. Interfaces* **2024**, *16*, 14742–14749.

[36] Dinda, S.; Karmakar, A.; Ghoshal, D.; Kundu, S. Redox insights and OER activity in 3D-MOFs: The role of alkali metal ions. *J. Mater. Chem. A* **2024**, *12*, 8392–8404.

[37] Liang, J.; Gao, X. T.; Guo, B.; Ding, Y.; Yan, J. W.; Guo, Z. X.; Tse, E. C. M.; Liu, J. X. Ferrocene-based metal-organic framework nanosheets as a robust oxygen evolution catalyst. *Angew. Chem. Int., Ed.* **2021**, *60*, 12770–12774.

[38] Wu, J.; Yu, Z. J.; Zhang, Y. Y.; Niu, S. Q.; Zhao, J. Y.; Li, S. W.; Xu, P. Understanding the effect of second metal on CoM (M = Ni, Cu, Zn) metal-organic frameworks for electrocatalytic oxygen evolution reaction. *Small* **2021**, *17*, 2105150.

[39] Chang, G. R.; Zhou, Y. T.; Wang, J. H.; Zhang, H.; Yan, P.; Wu, H. B.; Yu, X. Y. Dynamic reconstructed RuO_2 /NiFeOOH with coherent interface for efficient seawater oxidation. *Small* **2023**, *19*, 2206768.

[40] Tan, W. L.; McNeill, C. R. X-ray diffraction of photovoltaic perovskites: Principles and applications. *Appl. Phys. Rev.* **2022**, *9*, 021310.

[41] Wen, Z. W.; Kim, W.; Yoo, S. J.; Chae, C. G.; Seo, H. B.; Bak, I. G.; Changez, M.; Lee, J. S. Highly ordered supramolecular structure built from poly(4-(4-vinylphenylpyridine)) and 1,1′ferrocenedicarboxylic acid via hydrogen bonding. *Polym. Chem.* **2020**, *11*, 2666–2673.

[42] Liu, Y. J.; Li, B. B.; Liu, Y. Y.; Cheng, X. F.; Liang, X. M.; Zhang, J. H.; Zhu, G. X. Sheet-like units of ferrocene-based coordination compounds for oxygen evolution. *Colloids Surf. A: Physicochem. Eng. Aspects* **2022**, *654*, 130070.

[43] Chen, K.; Cao, Y. H.; Yadav, S.; Kim, G. C.; Han, Z.; Wang, W. M.; Zhang, W. J.; Dao, V.; Lee, I. H. Electronic structure reconfiguration of nickel-cobalt layered double hydroxide nanoflakes via engineered heteroatom and oxygen-vacancies defect for efficient electrochemical water splitting. *Chem. Eng. J.* **2023**, *463*, 142396.

[44] Lin, R. J.; Kang, L. Q.; Zhao, T. Q.; Feng, J. R.; Celorrio, V.; Zhang, G. H.; Cibin, G.; Kucernak, A.; Brett. D. J. L.; Corà, F. et al. Identification and manipulation of dynamic active site deficiency-induced competing reactions in electrocatalytic oxidation processes. *Energy Environ. Sci.* **2022**, *15*, 2386–2396.

[45] Wei, J.; Xia, D. S.; Wei, Y. P.; Zhu, X. Y.; Li, J.; Gan, L. Probing the oxygen reduction reaction intermediates and dynamic active site structures of molecular and pyrolyzed Fe-N-C electrocatalysts by *in situ* Raman spectroscopy. *ACS Catal.* **2022**, *12*, 7811–7820.

[46] Bai, L. C.; Lee, S.; Hu, X. L. Spectroscopic and electrokinetic evidence for a bifunctional mechanism of the oxygen evolution reaction. *Angew. Chem. Int. Ed.* **2021**, *60*, 3095–3103.

[47] Zhao, L.; Yan, J. H.; Huang, H. J.; Du, X.; Chen, H.; He, X.; Li, W. X.; Fang, W.; Wang, D. H.; Zeng, X. H. et al. Regulating electronic structure of bimetallic NiFe-THQ conductive metal organic frameworks to boost catalytic activity for oxygen evolution reaction. *Adv. Funct. Mater.* **2024**, *34*, 2310902.

[48] Sun, S. F.; Zhou, X.; Cong, B. W.; Hong, W. Z.; Chen, G. Tailoring the d-Band Centers Endows $(Ni_xFe_{1-x})_2P$ nanosheets with efficient oxygen evolution catalysis. *ACS Catal.* **2020**, *10*, 9086–9097.